New Amorphous Mixed Transition Metal Oxides and Their Li Derivatives: Synthesis, Characterization, and Electrochemical Behavior

F. Leroux, Y. Piffard,* G. Ouvrard, J.-L. Mansot,[a†] and D. Guyomard

Institut des Matériaux Jean Rouxel, UMR CNRS-Université de Nantes No. 6502, 2, rue de la Houssinière, BP 32229 44322 Nantes Cedex 3, France

Received June 1, 1999. Revised Manuscript Received July 19, 1999

New amorphous $MnV_2O_{6+\delta}\cdot nH_2O$ ($0 < \delta < 1$) compounds have been prepared by a soft chemistry route including the precipitation of a crystallized precursor, $MnV_2O_6\cdot 4H_2O$, and its ozonation at temperatures below 100 °C. A combination of techniques (TGA, magnetic measurements, IR, XANES, EXAFS, XPS, and EELS) was used for their characterization. At low voltage, very large amounts of Li (e.g., $Li_{12}MnV_2O_{6.96}$) are stored into anhydrous $MnV_2O_{6+\delta}$ compounds. After the first Li uptake, subsequent charge/discharge cycles correspond to fully reversible Li uptake between the two compositions: $Li_\alpha MnV_2O_{6+\delta}$ ($\alpha \geq 2$) and $Li_{12}MnV_2O_{6+\delta}$ (from 600 to 900 mAh/g). The Li derivatives were characterized at various steps of the discharge/charge process. During the first discharge the VO_n polyhedron changes from VO_5 to VO_6, and reversibly from VO_6 to VO_4 during subsequent cycles. Meanwhile, the V oxidation state varies reversibly between +3 and +5, respectively. Upon the first discharge Mn^{4+} cations are reduced to Mn^{2+}. During the subsequent cycles the average Mn oxidation state varies reversibly between +2 and ∼+2.6. The electron transfer from Li to the host matrix is shown to decrease with increasing Li uptake. It is shown that the same soft chemistry route enables the preparation of amorphous $CoV_2O_{6+\delta}\cdot nH_2O$ ($0 < \delta < 1$) compounds which exhibit similar storage properties.

1. Introduction

The continued growth in the use of portable electronic equipment and the raising interest for the electric vehicle has led to an ever increasing demand for higher energy and power density, rechargeable batteries. Consequently, many studies are presently being devoted to the improvement of battery performance. In this area, lithium batteries and more precisely electrode materials for such batteries, i.e., compounds which exhibit Li intercalation/deintercalation properties, are attracting a great deal of research; see for example ref 1. This is mainly true for compounds that can be used as positive electrode materials. However, with a growing interest for Li ion batteries[2] that use a Li intercalation compound as a negative electrode, a clear revival of the research on such materials is being observed.[3−11]

Among cathode materials, manganese, and vanadium oxides have been and are still intensively studied. With the aim of obtaining new cathode materials, investigations in the Mn−V−O system have been undertaken under oxidizing conditions. As it will be seen below, they can lead to compounds with quite unexpected electrochemical behavior.

In this paper, we report the synthesis, by soft chemistry routes, of new amorphous mixed oxides with the formulation $MnV_2O_{6+\delta}\cdot nH_2O$ ($0 < \delta < 1$) and their characterization. Furthermore, the electrochemical behavior of these materials with respect to lithium storage is described along with a detailed characterization of the lithiated derivatives, mainly by local techniques. Finally, an extension of the preparation technique to the synthesis of $CoV_2O_{6+\delta}\cdot nH_2O$ is presented and preliminary results of its electrochemical behavior are given.

2. Experimental Details

2.1. Synthesis. $MnV_2O_{6+\delta}\cdot nH_2O$ ($0 < \delta < 1$) amorphous mixed oxides were prepared by a two-step process: the preparation of a crystallized precursor $MnV_2O_6\cdot 4H_2O$[12] and ozonation at temperatures below 100 °C.

* To whom correspondence should be addressed. E-mail: piffard@cnrs-imn.fr.

† Present address: Département de Physique, Faculté des Sciences, Campus Fouillole, 97159 Pointe à Pitre.

(1) Extended Abstracts of 9th International Meeting on Lithium Batteries, July 1998, Edinburgh, Scotland, UK.

(2) Rechargeable Lithium Batteries. *Solid State Ionics* **1994**, *69*, 173−265.

(3) Nishijima, M.; Kagohashi, T.; Takeda, Y.; Imanishi, M.; Yamamoto, M. *J. Power Sources* **1997**, *68*, 510−514.

(4) Shodai, T.; Okada, S.; Tobishima, S.; Yamaki, J. *J. Power Sources* **1997**, *68*, 515−518.

(5) Yoshio, I.; Masayuki, M.; Yukio, M.; Tadahiko, K.; Tsutomu, M. European Patent No. 0 651 450 A1; filed on Oct 21, 1994.

(6) Idota, Y.; Kubota, T.; Matsufuji, A.; Maekawa, Y.; Miyasaka, T. *Science* **1996**, *276*, 1396.

(7) Courtney, I. A.; Dahn, J. R. *J. Electrochem. Soc.* **1997**, *144*, 2943.

(8) Guyomard, D.; Sigala, C.; Le Gal La Salle, A.; Piffard, Y. *J. Power Sources* **1997**, *68*, 692−697.

(9) Piffard, Y.; Leroux, F.; Guyomard, D.; Mansot, J.-L.; Tournoux, M. *J. Power Sources* **1997**, *68*, 698−703.

(10) Denis, S.; Baudrin, E.; Touboul, M.; Tarascon, J.-M. *J. Electrochem. Soc.* **1997**, *144*, 4099.

(11) Leroux, F.; Goward, G. R.; Power, W. P.; Nazar, L. F. *Electrochem. Solid State Lett.* **1998**, *1*, 255.

10.1021/cm991074g CCC: $18.00
Published on Web 09/23/1999

2.1.1. Preparation of $MnV_2O_6 \cdot 4H_2O$. $MnV_2O_6 \cdot 4H_2O$ was prepared as previously mentioned in the literature[12] by mixing equal volumes of aqueous solutions of $NaVO_3$ (2×10^{-2} M) and manganese nitrate, $Mn(NO_3)_2 \cdot 4H_2O$ (10^{-2} M) at room temperature (RT). The formation of the precipitate occurred rapidly and was accelerated by mechanical stirring and/or bubbling with air. In the course of this study, we obtained single crystals of $MnV_2O_6 \cdot 4H_2O$ by keeping the solution between 65 and 95 °C overnight, thus allowing a crystal structure determination.[13]

2.1.2. Ozonation of $MnV_2O_6 \cdot 4H_2O$. The ozonation of the crystallized precursor was undertaken at various temperatures lower than 100 °C. (Ozone is rapidly decomposed above this temperature.) The use of ozone for the preparation of amorphous V_2O_5 (from a solution of $VOSO_4$)[14] or of MnO_2,[15,16] has previously been reported. Ozone was produced according to the method proposed by Berthelot:[17] an oxygen stream was submitted to a high discharge voltage by flowing through a Labo100 Dixwell apparatus which then produced a O_2/O_3 mixture containing about 5% ozone. For the ozonation experiment the precursor was placed in a tubular furnace through which the oxidizing mixture was flowing. Samples were heated in that manner for about 36 h leading to $MnV_2O_{6+\delta} \cdot nH_2O$ products.

2.2. Characterization. A combination of TGA, magnetic measurements, and several spectroscopies (IR, XANES, EXAFS, XPS, and EELS) was used to characterize the $MnV_2O_{6+\delta} \cdot nH_2O$ materials and their Li derivatives.

2.2.1. TGA. Thermal analyses were made on a Setaram TG-DSC 111 system equipped with a Leybold Mass Spectrometer, at a heating rate of 1 K/min.

2.2.2. Magnetic Studies. Magnetic measurements were conducted on a Quantum Design SQUID magnetometer with the use of powdered samples (~50 mg), first cooled to 5 K at zero field and then warmed to 300 K under an applied field of 5 kOe. The data were corrected for contributions from sample holder, background, and core diamagnetism. The susceptibility was defined as the ratio of the magnetization M to the applied field H (χ = M/H), and effective magnetic moments were obtained from $\mu_{eff}/\mu_B = 2.828\ (\chi T)^{1/2}$, with χ expressed in electromagnetic units per mole (emu/mol).

2.2.3. XPS. A Leybold LHS12 ESCA unit was used to record the XPS spectra (XPS mode; focused monochromatized Mg Kα radiation, 1253.6 eV; residual pressure inside the analysis chamber, $\sim 5 \times 10^{-8}$ Pa). The binding energy was scaled with the C 1s line (284.6 eV) from the carbon contamination layer.

2.2.4. Infrared Studies. IR spectra were obtained on a 20SCX FTIR spectrometer with the use of KBr pellets.

2.2.5. X-ray Absorption Analysis. X-ray absorption spectra were recorded at LURE (the French synchrotron source), on the DCI storage ring using 1.85 GeV positrons with an average current intensity of 250 mA. They were collected in transmission mode at the V and Mn k edges, on the EXAFS III spectrometer. A double-crystal Si(311) monochromator was used and harmonic rejection was performed by a detuning of the Si crystals until the intensity of the beam after passing through the monochromator had decreased by 40%. The flux before and after entering the cell was measured by helium−neon and air-filled ionization chambers, respectively. The monochromator calibration was performed at the first inflection point of the V and Mn k edges with 6μm V and Mn foils, respectively. The spectra of these metallic foils were recorded either before or after each unknown spectrum to allow further energy calibration.

Each material was powdered, uniformly dispersed in boron nitride powder and sandwiched between two X-ray transparent Kapton adhesive tapes. The electrochemical cells used for lithium insertion/deinsertion were opened in a glovebox and the composite materials were vacuum-dried and introduced in an Ar-containing bin for XAS analysis.

The XANES spectra were recorded by steps of 0.2 eV with 1 s of accumulation time per point within the 5430−5550 eV and 6510−6630 eV energy ranges for V and Mn k edges, respectively. The EXAFS spectra were recorded in the same way within a 1000 eV energy range, 5350−6350 eV and 6430−7430 eV for V and Mn k edges respectively, with 2 eV steps and 2 s of accumulated time per point.

All XANES spectra were analyzed following the same method. After energy calibration, the background was subtracted by extrapolation of the preedge absorption using a Victoreen function. The absorption was then normalized by taking, as unity, the absorbance value at the midpoint of the first EXAFS oscillation. The zero of the photon energy scale was taken with respect to the first inflection point of the transition metal derivative spectrum (i.e., 5465 and 6539 eV for V and M metals, respectively).

The EXAFS analysis was performed following the single scattering theory[18,19] using the software written by Michalowicz.[20] The background absorption was calculated using a theoretical expression developed by Lengeler and Eisenberger,[21] and the single atomic absorption of the absorber was interpolated by a fourth- or fifth-degree polynomial between 5480 and 6350 eV for V, and between 6550 and 7430 eV for Mn. Each spectrum was carefully extracted by varying both the degree and first point of the polynomial, and the best removal of low-frequency noise was checked by further Fourier transformation. The energy of the edge, E_0, was taken as being equal to that of the half-height of the absorption. The pseudo-radial distribution function (RDF) around the central atom was obtained by a Fourier transform of the weighted $\omega(k)k^3\chi(k)$ spectra, where $\omega(k)$ is a window using a Kaiser function (τ = 2.5) defined between 3 and 12 Å^{-1}. All the further back-Fourier transforms included a subtraction of this window. The refinements were performed by fitting the structural parameters using both simplex and least-squares calculations.[22] These structural parameters are N, the number of neighbors of a defined species around the central atom, at the distance R with both thermal and structural disorder expressed through σ, the Debye−Waller factor. Previous assumptions[19] indicated that the errors can be taken to be equal to 0.3 eV for the energy, 20% for N, 0.03 Å for R, and 0.02 Å for σ. The fits were performed with a reliance level of 65%. Fitting procedures have been performed with the use of the amplitude and phase functions from Feff7.[23]

2.2.6. Electron Energy Loss Spectroscopy (EELS). Experiments were carried out on a Philips CM30 microscope running at 150 kV with an undersaturated LaB_6 cathode.

EELS spectra were recorded in the diffraction coupling mode with the use of a GATAN 666 parallel spectrometer.

The condenser, objective, and spectrometer entry aperture diameters were respectively 150 μm, 70 μm, and 2 mm, leading to collection half-angle of 12 mrad and an energy resolution of 9.9 eV (fwhm of the zero loss peak). EELS spectra were recorded with an energy dispersion of 0.1 eV per channel on circular areas of 1−5 μm diameter, the total irradiation dose lying in the 50−500 e/Å^2 range for one spectrum.

The energy position of edges for an element strongly depends on its valence state.[24−26] In the case of transition metal (TM) cations, the relative intensities of the l_3 and l_2 white lines

(12) Zolotavin, V. L.; Bulygina, V. N.; Bezrukov, I. Ya. *Russ. J. Inorg. Chem.* **1970**, *15* (2), 222.
(13) Liao, J.-H.; Drezen, T.; Leroux, F.; Guyomard, D.; Piffard, Y. *Eur. J. Solid State Inorg. Chem.* **1996**, *33*, 411.
(14) Sato, Y.; Matsueda, N.; Tokugawa, H.; Kobayakawa, K. *Chem. Lett.* **1993**, 901.
(15) Faber, P.; Brenet, J. German Patent 2419490, 1968.
(16) Faber, P. *Chem. Eng. Technol.* **1977**, *49*, 333.
(17) Berthelot. *Compt. Rev.* **1876**, *82*, 1261.
(18) Lytle, F. W.; Sayers, D. E.; Stern, E. A. *Phys. Rev.* **1975**, *11*, 4825.
(19) Teo, B. K. *EXAFS: Basic principles and analysis*; Springer: Berlin, 1986.
(20) Michalowicz, A. *Logiciels pour la Chimie*; Société Française de Chimie: Paris, 1991; p 102.
(21) Lengeler, B.; Eisenberger, P. *Phys. Rev. B* **1980**, *21*, 4507.
(22) James, F.; Roos, M. *MINUIT*, CERN computing center, Program Library, CERNID Internal Report 75/20, 1976.
(23) Rehr, J. J. *Jpn. J. Appl. Phys.* **1993**, *32*, 8.

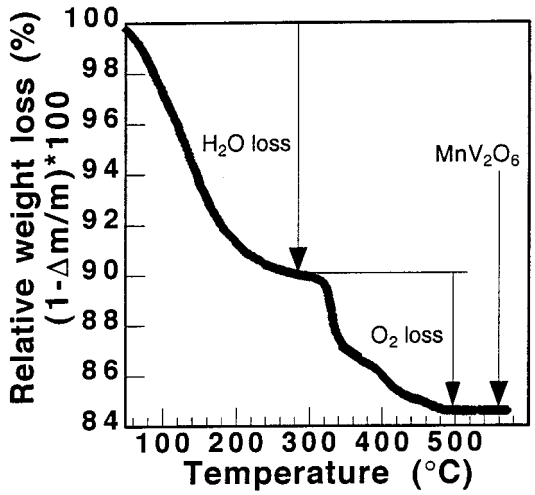

Figure 1. TG curve of $MnV_2O_{6+\delta}\cdot nH_2O$ prepared at 95 °C.

($2p_{3/2} \rightarrow 3d_{3/2},3d_{5/2}$ and $2p_{1/2} \rightarrow 3d_{3/2}$) are highly sensitive to the 3d occupancy. The energy positions of manganese and vanadium l_3 edges and the l_3/l_2 white line ratios were then used to determine the oxidation states of the TM cations in the materials.

3. Characterization of $MnV_2O_{6+\delta}\cdot nH_2O$ Compounds

The soft chemistry route leading to the $MnV_2O_{6+\delta}\cdot nH_2O$ compounds suggests additional comments dealing with the respective importance of both the crystallized precursor and the oxidizing agent. It must first be mentioned that if the anhydrous compound MnV_2O_6 (brannerite)[27] is used as the precursor, no oxidation occurs in the second step. Similarly, if pure oxygen is used instead of the O_3/O_2 mixture the $MnV_2O_6\cdot 4H_2O$ precursor remains intact. At temperatures between 60 and 100 °C, it has been shown that $MnV_2O_6\cdot 4H_2O$ undergoes a dehydration process leading to $MnV_2O_6\cdot 2H_2O$.[13] Therefore, at all ozonation temperatures, the precursor was hydrated. Consequently, it seems that both a hydrated precursor and the use of ozone are required in the synthetic route.

X-ray and electron diffraction experiments show that all $MnV_2O_{6+\delta}\cdot nH_2O$ materials are amorphous.

3.1. Thermal Behavior. The thermal behavior of the material prepared at 95 °C is illustrated in Figure 1 and is representative of the other members. The TG curve shows two distinct weight loss processes: The first occurs between RT and 300 °C. It is reversible and corresponds to a water loss. The second, observed between 320 and 500 °C, is irreversible and corresponds to an oxygen loss. It leads to the brannerite compound MnV_2O_6.

On account of the TG results the chemical formulas $MnV_2O_{6+\delta}\cdot nH_2O$ (Table 1) can be proposed. They show that as the ozonation temperature is increased, the hydration rate decreases whereas the average oxidation state of Mn increases. [we assume here that V retains its original oxidation state (+5) as this will be shown by spectroscopic measurements.]

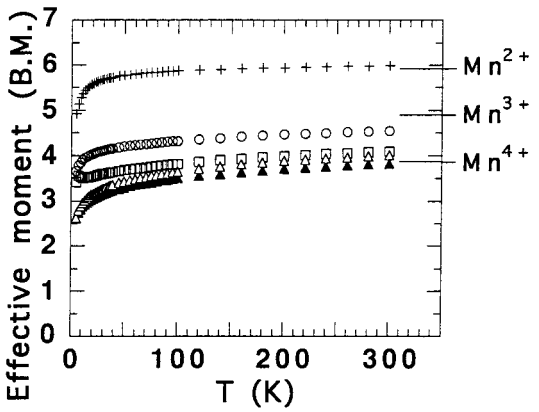

Figure 2. Temperature dependencies of the effective magnetic moments of the precursor material $MnV_2O_6\cdot 4H_2O$ (crosses) and of $MnV_2O_{6+\delta}\cdot nH_2O$ materials prepared at 25 °C (open circles), 35 °C (open squares), 65 °C (open triangles), and 95 °C (filled triangles).

Table 1. $MnV_2O_{6+\delta}\cdot nH_2O$ Chemical Formulas Inferred from TGA and Average Oxidation State of Mn Inferred from TGA and EELS

ozonation temperature (°C)	chemical formula	oxidation state of Mn from TGA	oxidation state of Mn from EELS (l_3/l_2 intensity ratio)
25	$MnV_2O_{6.58}\cdot 3.4H_2O$	3.16	3.1 ± 0.2
35	$MnV_2O_{6.81}\cdot 2.5H_2O$	3.62	3.4 ± 0.2
65	$MnV_2O_{6.90}\cdot 2.1H_2O$	3.80	3.6 ± 0.2
95	$MnV_2O_{6.96}\cdot 1.7H_2O$	3.92	4.0 ± 0.2

3.2. Magnetic Study. The temperature dependencies of the effective magnetic moment $\mu_{eff}(T)$ are shown in Figure 2. The spin-only magnetic moments for Mn^{2+}, Mn^{3+}, and Mn^{4+} (5.92, 4.90, and 3.87 μ_B, respectively) are shown for comparison. At high temperature, say above 100 K, the effective moments are slightly temperature dependent. In this region, the plot of Figure 2 clearly shows that ozonation leads to magnetic moments lower than that of the precursor, and this can be unambiguously related to the oxidation of the manganese species upon ozonation. For the highest ozonation temperature, the oxidation could even yield to a compound with only Mn^{4+}.

3.3. Spectroscopic Analyses. *3.3.1. XPS.* XPS spectra corresponding to the 2p, 3p, and 3s energy levels of both Mn and V in $MnV_2O_{6.96}\cdot 1.7H_2O$ were recorded and compared with those of the reference compounds: the precursor $MnV_2O_6\cdot 4H_2O$ and MnV_2O_6 (brannerite).

As expected for a vanadium cation remaining in a +5 oxidation state, the $2p_{1/2}$ and $2p_{3/2}$ peaks appear at the same energy in the three compounds (Figure 3), and this is also the case for the 3p and 3s peaks (Figures 4 and 5). In contrast, all Mn peaks in $MnV_2O_{6.96}\cdot 1.7H_2O$ are shifted with respect to those of the reference compounds: In the reference compounds, the $2p_{3/2}$ peak appears at 641.5 eV, with an energy splitting $2p_{1/2}-2p_{3/2}$ of 11.7 eV, and satellite peaks are observed at 5.5 eV to higher energies than these main peaks as expected for compounds containing Mn^{2+} (Figure 6).[28,29] The Mn 2p

(24) Egerton, R. F. *EELS in the electron microscope*; Plenum Press: New York, 1986.
(25) Brown, M.; Peierls, R. E.; Stern, E. A. *Phys. Rev. B* **1977**, *15*, 738.
(26) Leapman, R. D.; Grunes, L. A.; Feyes, P. L. *Phys. Rev. B* **1982**, *26*, 614.
(27) Müller-Buschbaum, Hk.; Kobel, M. *J. Alloys Compounds* **1991**, *176*, 39.
(28) Chen, X. M.; Clearfield, A. *J. Solid State Chem.* **1986**, *64*, 270.
(29) Baltanas, M. A.; Katzer, J. R.; Stiles, A. B. *Acta Chim. Acad. Sci. Hung.* **1987**, *124*, 341.

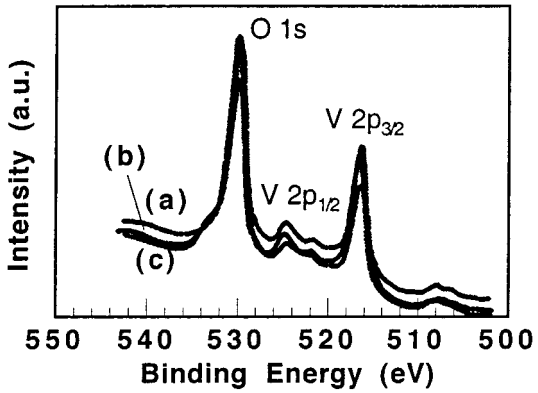

Figure 3. V 2p XPS spectra of $MnV_2O_6{\cdot}4H_2O$ (a), MnV_2O_6 (b), and $MnV_2O_{6.96}{\cdot}1.7H_2O$ (c).

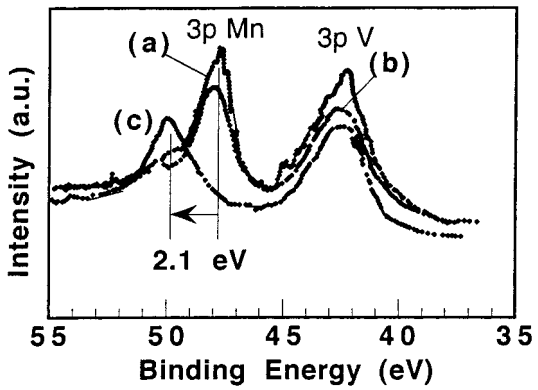

Figure 4. V and Mn 3p XPS spectra of $MnV_2O_6{\cdot}4H_2O$ (a), MnV_2O_6 (b), and $MnV_2O_{6.96}{\cdot}1.7H_2O$ (c).

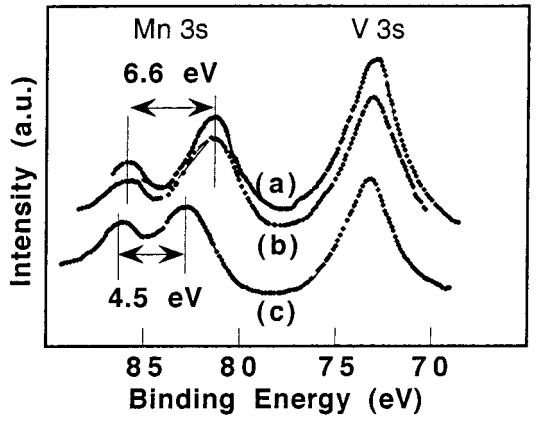

Figure 5. V and Mn 3s XPS spectra of $MnV_2O_6{\cdot}4H_2O$, (a) MnV_2O_6 (b), and $MnV_2O_{6.96}{\cdot}1.7H_2O$ (c).

spectrum of $MnV_2O_{6.96}{\cdot}1.7H_2O$ does not show such satellite peaks. Furthermore, the $2p_{3/2}$ peak is shifted by +1.2 eV with respect to that of the reference compounds and a similar shift is observed between the Mn $2p_{3/2}$ peaks in MnO and MnO_2.[30] The binding energy of the Mn 3p level, sensitive both to the environment and the oxidation state, clearly confirms an increase of the Mn oxidation state due to the ozonation: the Mn 3p peak is at 47.9 eV in the reference compounds, whereas it appears at 50 eV in $MnV_2O_{6.96}{\cdot}1.7H_2O$ (Figure 4). This latter value is that observed for the 3p level of Mn^{4+}, with an octahedral coordination, in

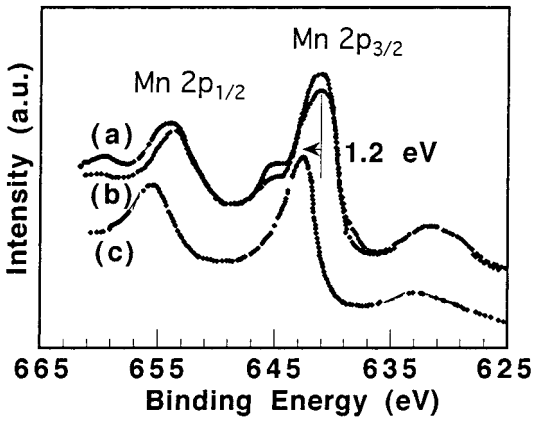

Figure 6. Mn 2p XPS spectra of $MnVO_6{\cdot}4H_2O$, (a) MnV_2O_6 (b), and $MnV_2O_{6.96}{\cdot}1.7H_2O$ (c).

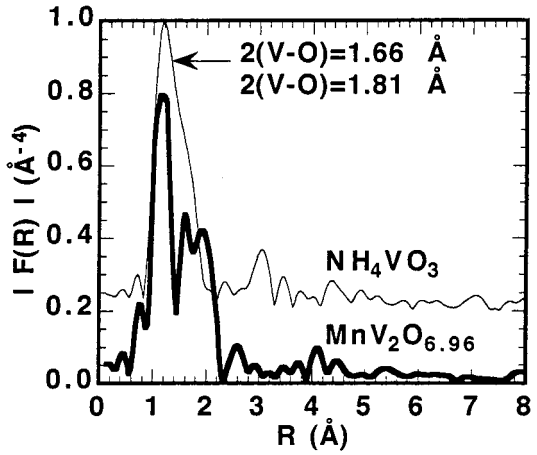

Figure 7. Modulus of the EXAFS spectra Fourier transform (V k edge) of NH_4VO_3 and $MnV_2O_{6.96}$. (The distances are not corrected for atomic potential phase shifts.)

$NiMnZnO_4$.[31] The energy position and the multiplet splitting energy values of the 3s levels can be predicted by the Van Vleck's theorem.[32] For $3d^n$ transition elements, it has been shown that the multiplet splitting energy depends on n.[25] It decreases by about 1 eV per electron with a maximum value of 7 eV for a $3d^5$ cation (Mn^{2+}). For $MnV_2O_{6.96}{\cdot}1.7H_2O$ the Mn 3s energy splitting is 2.1 eV smaller than that of the Mn^{2+} reference compounds (Figure 5) and then consistent with reported values for $3d^3$ electronic configurations.[33]

3.3.2. EXAFS. A comparison of the vanadium RDFs of $MnV_2O_{6.96}$ and NH_4VO_3 clearly shows that the vanadium coordination polyhedra in these two compounds are different (Figure 7). The VO_4 tetrahedron of NH_4VO_3, with two types of V−O distances, leads to a large peak, whereas three distinct peaks are observed for $MnV_2O_{6.96}$. Their refinement leads to three V−O distances very close to those encountered in the precursor $MnV_2O_6{\cdot}4H_2O$ and a number of neighbors close to 5 (see results of the fits in the k space summarized in Table 2). It appears therefore that the ozonation does not change the arrangement of the first shell around the V atoms.

(30) Wagner, C. D.; Riggs, W. M.; Davis, L. E.; Moulder, J. F.; Muilenberg, G. E. *Handbook of X-ray Photoelectron Spectroscopy*; Perkin-Elmer Corporation: Eden Prairie, MN, 1979.

(31) Brabers, V. A. M.; Van Setten, F. M.; Knapen, P. S. A. *J. Solid State Chem.* **1983**, *49*, 93.
(32) Van Vleck, J. H. *Phys. Rev.* **1934**, *45*, 405.
(33) Shirley, D. A. *Phys. Scr.* **1975**, *11*, 117.

Table 2. Results of the Fits for the First V and Mn Coordination Shells in $MnV_2O_{6.96}$ (Inferred from EXAFS Experiments)[a]

	d (Å)	N	$\sigma \times 10^{-2}$ (Å)	ΔE (eV)	ρ (%)
	1.65	2.0			
V−O	1.90	1.8	5	8.2	5
	2.06	1.0			
Mn−O	1.895	4.2	8	6.5	0.8

[a] Abbreviations: *N* is the number of oxygen atoms surrounding the absorbing atom (V or Mn), σ is the Debye−Waller factor, and ΔE and ρ represent the edge variation and the reliability factor of the fit.

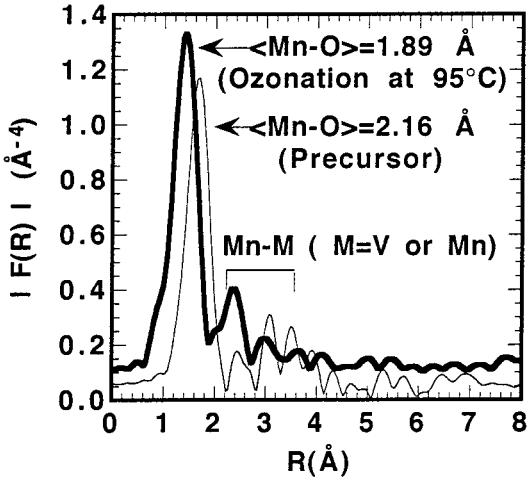

Figure 8. Modulus of the EXAFS spectra Fourier transform (Mn k edge) of $MnV_2O_6 \cdot 4H_2O$ and $MnV_2O_{6.96}$. (The distances are not corrected for atomic potential phase shifts.)

A comparison of the manganese RDFs of $MnV_2O_{6.96}$ and $MnV_2O_6 \cdot 4H_2O$ clearly shows a shift of the Mn−O peak for $MnV_2O_{6.96}$ toward shorter Mn−O distances (Figure 8). The refinement leads to a Mn−O distance of 1.895 Å in fair agreement with Mn^{4+} in a 6-fold coordination, even though the number of neighbors refined is only 4.2 (Table 2). On account of the errors in the determination of this number and, as will be shown below by the intensity of the preedge peak of the XANES spectrum, the expected number of neighbors, i.e., 6, is not in doubt.

3.3.3. XANES. The vanadium k-edge XANES spectra of $MnV_2O_{6.96}$ and of the precursor material are displayed in Figure 9. An intense preedge peak is observed for both compounds. It corresponds to an electron transition from the core level (1s) to the p symmetry part of the first non completely filled energy level (molecular orbital mainly V 3d type in the case of the vanadium k edge). As a consequence, its intensity is indicative of a noncentrosymmetric environment of vanadium atoms. Furthermore, the width of the preedge peak, which is correlated to the spread of V−O distances,[34] is almost the same (∼2.5 eV) in $MnV_2O_{6.96}$ and $MnV_2O_6 \cdot 4H_2O$. The energy position of the edge-jump as well as that of the weak peaks in the continuum are very similar in $MnV_2O_{6.96}$ and $MnV_2O_6 \cdot 4H_2O$.

The Mn k-edge preedge spectra of MnO, Mn_2O_3, MnO_2 (IBA no. 15), and $MnV_2O_{6.96}$ are displayed in Figure 10. For all compounds the weak intensity of the preedge peak indicates that Mn occupies a symmetrical site.

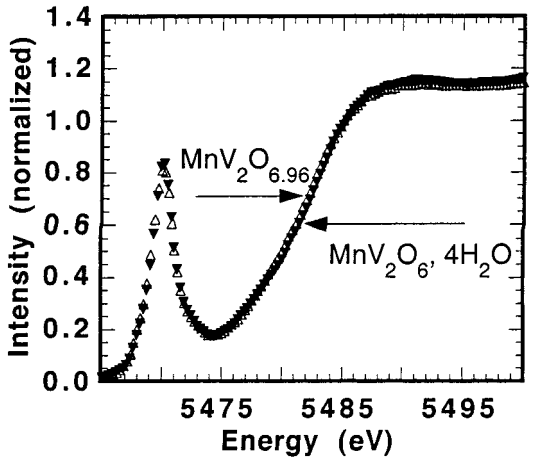

Figure 9. Normalized V k-edge XANES spectra of $MnV_2O_6 \cdot 4H_2O$ and $MnV_2O_{6.96}$.

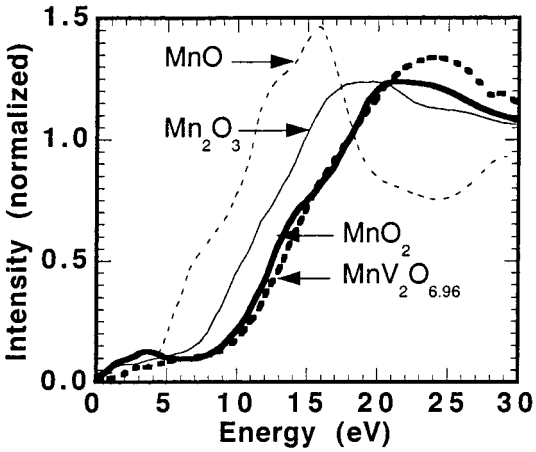

Figure 10. Normalized Mn k-edge XANES spectra of MnO, Mn_2O_3, MnO_2, and $MnV_2O_{6.96}$.

Furthermore, the edge-jumps for MnO_2 (IBA no. 15) and $MnV_2O_{6.96}$ are very close to each other. Such results are in good agreement with those of EXAFS studies, indicating that $MnV_2O_{6.96}$ contains Mn^{4+} in a 6-fold coordination.

3.3.4. EELS. Figure 11 enables a comparison of the energy positions and intensities of the V and Mn $l_{2,3}$ peaks in $MnV_2O_6 \cdot 4H_2O$, MnV_2O_6, and the various $MnV_2O_{6+\delta} \cdot nH_2O$ materials. As expected the V l edge spectra are nearly the same in all compounds, whereas a slight shift of the Mn l edges toward higher energies is observed when the ozonation temperature increases. Accordingly, the white line l_3/l_2 intensity ratio decreases, confirming an increase of the Mn oxidation state. Figure 12 shows the evolution of the white line l_3/l_2 intensity ratio as a function of the oxidation state of Mn in MnO, Mn_2O_3, and MnO_2.[35] From this graph, average oxidation states can be proposed for Mn in $MnV_2O_{6+\delta} \cdot nH_2O$ materials (Table 1). They are in fair agreement with those inferred from TG experiments.

3.3.5. IR. In addition to the lack of long-range order in the $MnV_2O_{6+\delta} \cdot nH_2O$ materials, as revealed by the diffraction experiments, it appears that the ozonation induces changes in the organization at short distance; as a matter of fact, IR absorption bands in the 400−

(34) Wong, J.; Lytle, F. W.; Messner, R. P.; Maylotte, D. H. *Phys. Rev. B* **1984**, *30*, 5596.

(35) Mansot, J.-L.; Leone, P.; Euzen, P.; Palvadeau, P. *Microsc. Microanal. Microstruct.* **1994**, *5*, 79.

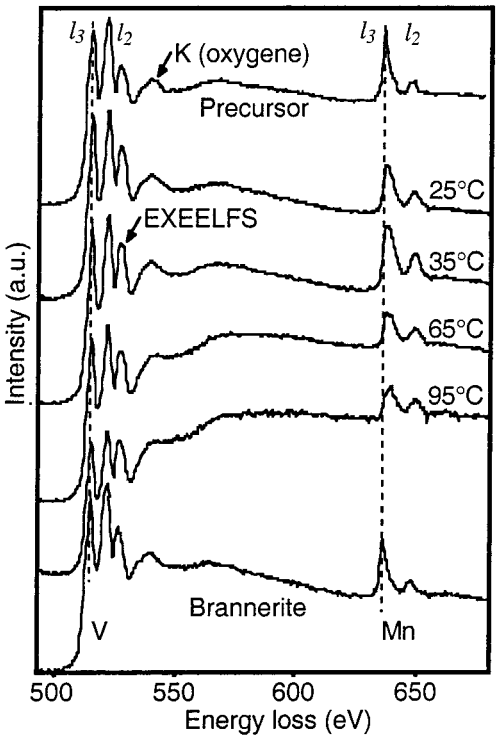

Figure 11. V and Mn $l_{2,3}$ edges for $MnV_2O_6{\cdot}4H_2O$ (precursor material), $MnV_2O_{6+\delta}{\cdot}nH_2O$ compounds (indicated by their ozonation temperature), and MnV_2O_6 (brannerite).

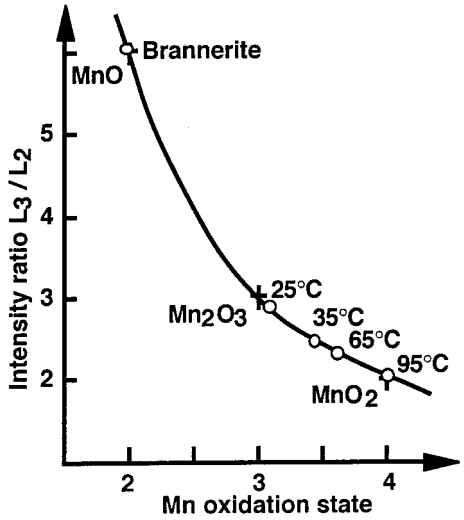

Figure 12. Variation of the Mn l_3/l_2 intensity ratio as a function of Mn oxidation state in reference compounds (crosses). $MnV_2O_{6+\delta}{\cdot}nH_2O$ compounds (open circles) are indicated by their ozonation temperature.

1000 cm^{-1} range, which are representative of V−O and Mn−O vibrations, are considerably broadened (Figure 13), thus indicating a larger distribution of V−O and Mn−O distances than in crystalline materials.

For V_2O_5 (Figure 13), it has previously been shown[36] that the vibration at 1000 cm^{-1} corresponds to the stretching mode of the short V═O bond, whereas that at 825 cm^{-1} is assigned to longer bonds. Similarly, the absorption band at 893 cm^{-1} in MnV_2O_6 can be assigned to the short V−O bonds (1.665 and 1.679 Å), while that at 791 cm^{-1} could correspond to the V−O bonds of 1.86

(36) Gilson, T. F.; Bizri, O. F.; Cheetham, N. *J. Chem. Soc., Dalton Trans.* **1973**, 291.

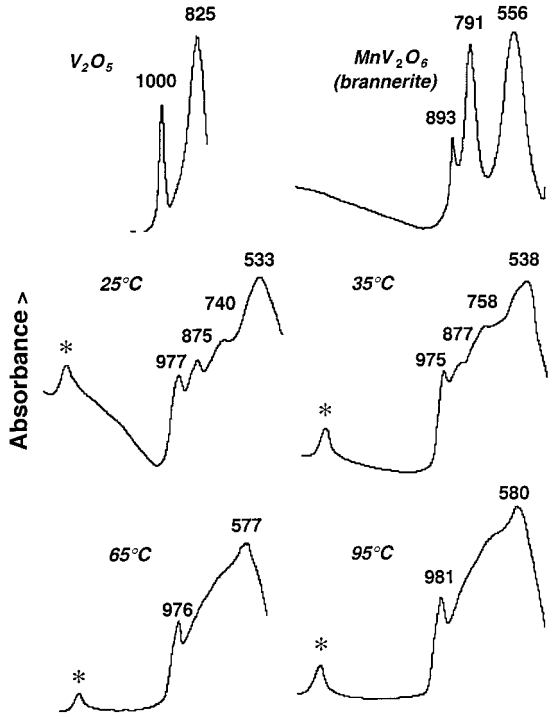

Figure 13. IR spectra of V_2O_5, MnV_2O_6, and $MnV_2O_{6+\delta}{\cdot}nH_2O$ compounds (indicated by their ozonation temperature). (The asterisk indicates O−H vibration.)

Å. The Mn−O bonds, which are longer, as well as the fifth V−O bond (2.094 Å) could be assigned to the absorption band observed at 556 cm^{-1}.

In $MnV_2O_{6+\delta}{\cdot}nH_2O$ materials, the very broad absorption domain of M−O bonds is delimited by rather well-defined bands at 978 ± 3 and 560 ± 30 cm^{-1}. The former clearly indicates the contribution of short V−O bonds such as those inferred from the EXAFS treatment. The latter, likely related to (at least) Mn−O vibrations, moves toward higher frequencies as the ozonation temperature increases in agreement with a decrease of the Mn−O distances when the oxidation state of manganese increases.

4. Electrochemical Behavior

4.1. Experimental. Composite electrodes were prepared by mixing the active material, a carbon black (Super-S from Chemetals Inc., Baltimore, MD), and a binder (poly(vinylidene difluoride), PVDF) with the mass ratio 85:10:5. The mixture was coated onto a stainless steel disk serving as the current collector. Electrodes had a surface area of 1 cm^2 and were between 2 and 5 mg/cm^2 of active material. Such prepared electrodes were evacuated at 100 °C for 2 h to remove adsorbed moisture, prior to entering the Ar-filled drybox for assembling the test cells.

Standard laboratory swagelok test cells were used with the composite electrode as the positive and Li metal as the negative, separated with glass paper soaked in the electrolyte.

The electrolyte was made of 1 M $LiClO_4$ dissolved in a 2:1 mixture of ethylene carbonate (EC) and dimethyl carbonate (DMC). The solvents and salt were purified and dried according to conventional procedures.

Swagelock cells were tested using the Mac-Pile system operating in a galvanostatic mode. The lithium composi-

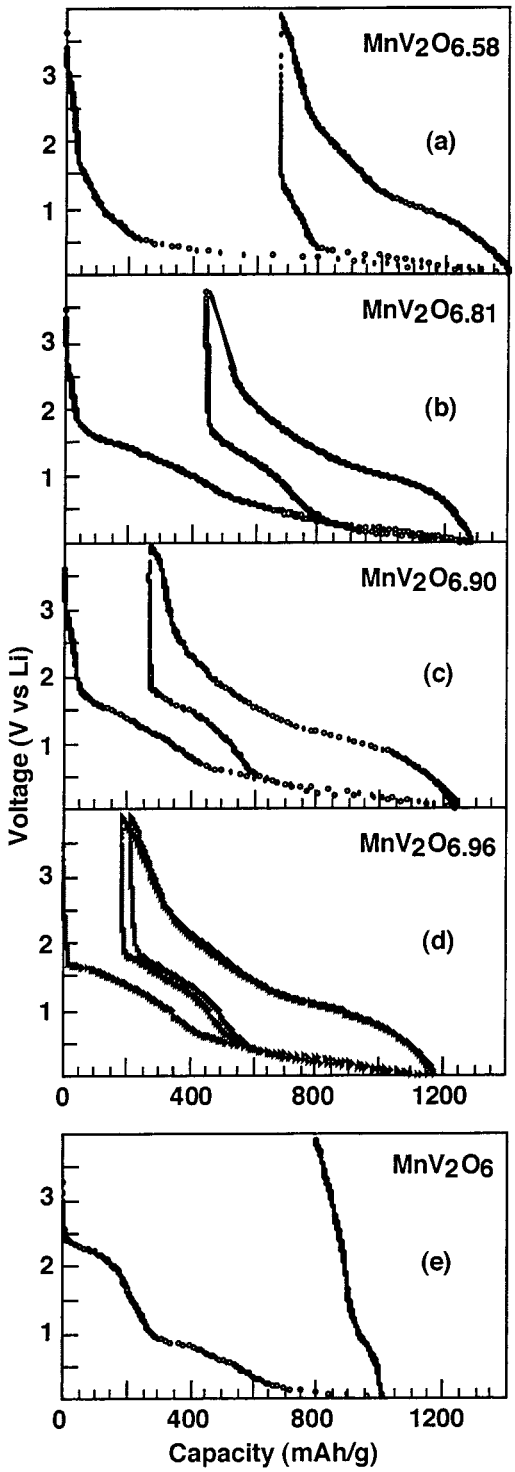

Figure 14. Voltage−capacity curves for composite electrodes $MnV_2O_{6+\delta}$ + C (10 wt %): (a) $\delta = 0.58$; (b) $\delta = 0.81$; (c) $\delta = 0.90$; (d) $\delta = 0.96$; and (e) MnV_2O_6 + C (10 wt %).

tion in the material was calculated from the elapsed time and the current, assuming that all the quantity of current is used in the uptake/extraction reaction.

4.2. Li Storage. As $MnV_2O_{6+\delta}\cdot nH_2O$ materials can be dehydrated without changing the oxidation state of the transition metal cations, all the electrochemical experiments were carried out on dehydrated materials.

Li storage in $MnV_2O_{6+\delta}$ compounds was investigated under galvanostatic conditions (C/20 rate); typical chronopotentiometric curves for the reduction and oxidation of $MnV_2O_{6+\delta}$ compounds are shown in Figure 14a−d.

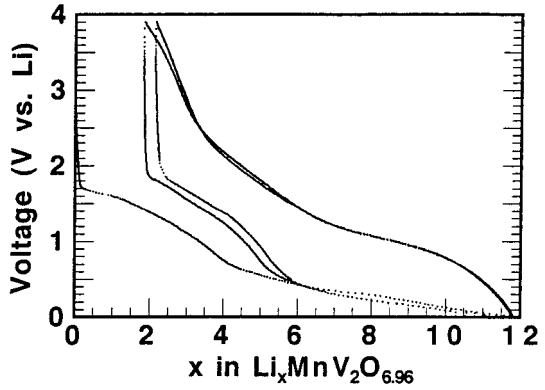

Figure 15. Intrinsic voltage−capacity curve for $MnV_2O_{6.96}$.

Contrary to all expectations, no Li uptake occurs above 1.7 V (vs Li); this behavior differs from the usual discharge curves of V^V and Mn^{IV} oxides, like MnO_2[37,38] and V_2O_5[39] reported in the literature.

The composite electrodes {$MnV_2O_{6+\delta}$ + C} exhibit a large capacity during the first discharge down to 10 mV (vs Li), and it is mostly recovered during the following charge, as shown in Figure 14a−d. It must be mentioned that within this voltage range, the Li uptake can also occur in the carbon black used to enhance the electronic conductivity of the composite electrode. To have access to the intrinsic electrochemical capacity of the material, the carbon contribution was withdrawn from the total capacity according to a method described in ref 40. The resulting chronopotentiometric curve for $MnV_2O_{6.96}$ is displayed in Figure 15. It shows that the first and second discharge curves exhibit similar shapes suggesting that during the first discharge down to 10 mV, the material undergoes a transformation which is mostly reversible. The intrinsic reversible capacity of $MnV_2O_{6.96}$ is about 10 Li per formula unit.

Figure 14 shows that Li can be stored reversibly in all $MnV_2O_{6+\delta}$ materials, with an irreversible loss of capacity in the course of the first discharge−charge cycle, a loss which increases when δ decreases. In MnV_2O_6 (Figure 14e), a first uptake step occurs at 2.4 V. It corresponds to two Li ions per formula unit and is likely to be related to the reduction of V^{5+} to V^{4+}. If the discharge is continued down to 10 mV, a large capacity is observed which however is not recovered during the next charge. For $MnV_2O_{6+\delta}$ materials, electrochemical data inferred from the chronopotentiometric curves are given in Table 3.

The second discharge and charge curves represented in Figure 15 show that the irreversible processes occur only for the first discharge. Similarly, irreversible processes occur at the first discharge with carbon black. In the latter case, this phenomenon is attributed to the formation of a passivation layer at the electrolyte/carbon interface. To know whether a similar interpretation could hold for $MnV_2O_{6+\delta}$ materials, incremental capacity curves were examined. Those for the first and second

(37) Leroux, F.; Guyomard, D.; Piffard, Y. *Solid State Ionics* **1995**, *80*, 307.
(38) Bach, S.; Pereira-Ramos, J.-P.; Baffier, N.; Messina, R. *Electrochem. Acta* **1991**, *36*, 1595.
(39) Delmas, C.; Cognac-Auradou, H.; Cocciantelli, J. M.; Menetrier, M.; Doumerc, J.-P. *Solid State Ionics* **1994**, *69*, 257.
(40) Guyomard, D.; Tarascon, J.-M. *J. Electrochem. Soc.* **1993**, *140* (11), 3071.

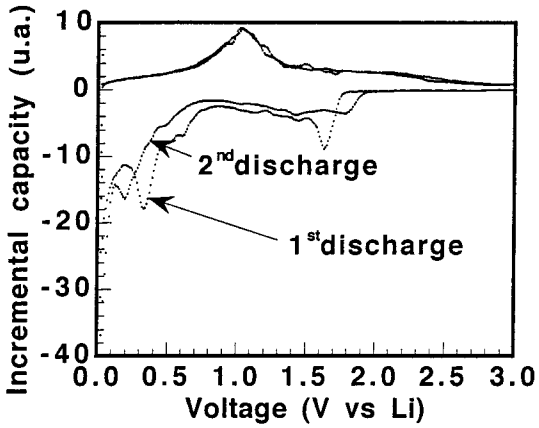

Figure 16. Incremental capacity curve for $MnV_2O_{6.96}$.

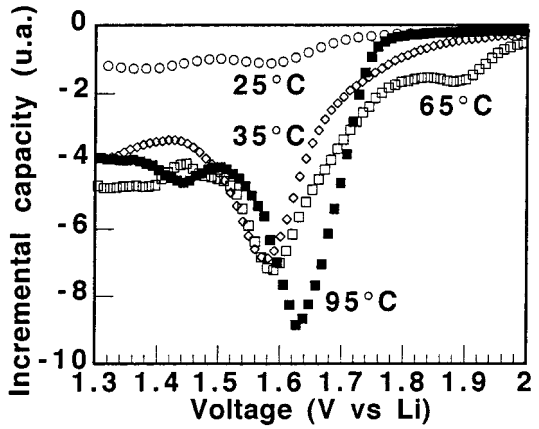

Figure 17. Incremental capacity curves in the 1.3−2 V voltage range for the $MnV_2O_{6+\delta}$ materials (indicated by their ozonation temperature).

Table 3. $MnV_2O_{6+\delta}$ Materials: Electrochemical Data in the 3.9−0.01 V Voltage Range

ozonation temperature (°C)	25	35	65	95
δ in $MnV_2O_{6+\delta}$	0.58	0.81	0.90	0.96
reversible specific capacity (mAh/g)	620	715	866	891
irreversible loss of capacity at first cycle (%)	50	35	29	15
average discharge voltage (V) (second discharge)	0.3	0.5	0.5	0.5
average charge voltage (V) (first charge)	1.1	1.5	1.5	1.5

discharge of $MnV_2O_{6.96}$ have been compared (Figure 16). The reduction peak at 1.6V on the first discharge curve is no longer observed on the second curve. However, a comparison of similar curves for the first discharge of all $MnV_2O_{6+\delta}$ materials (Figure 17) shows that the intensity of this peak decreases when the ozonation temperature decreases. This evolution is the opposite of that observed for the irreversible loss of capacity, and accordingly, it is not possible to make any conclusions at this level about the origin of the peak at 1.6V.

As the intensity of the 1.6 V reduction peak decreases when the ozonation temperature decreases (it moves also slightly toward lower voltages), the corresponding capacity Q_{irr}* was compared to the average oxidation state of manganese (the only variable parameter in the chemical formulation of $MnV_2O_{6+\delta}$ materials). Figure 18 shows a linear variation of Q_{irr}* (which was assimilated to the area of the peak) with the average oxidation state of manganese. Furthermore, it appears that the theoretical capacity corresponding to the Mn^{4+}/Mn^{3+} reduction, calculated from the chemical formulas given in Table 1, is very close to Q_{irr}* (Figure 18). On account of these results, one could then assume that the Mn^{4+}/Mn^{3+} reduction in $MnV_2O_{6+\delta}$ materials is an irreversible process which, consequently, traps Li ions within the materials. It will be seen below that XAS and EELS experiments confirm this interpretation which, nevertheless, remains a puzzling result if one considers that the reversible capacity also increases when the ozonation temperature increases, i.e., when the average oxidation state of Mn increases.

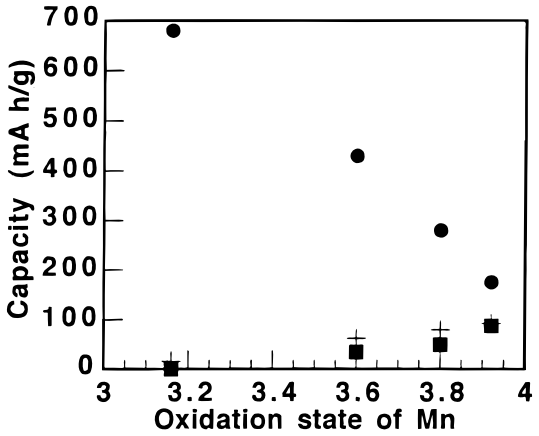

Figure 18. Variations of Q_{irr}* (filled squares) (area of the 1.6 V reduction peak) and of the total irreversible capacity (●) at first cycle, vs the oxidation state of manganese in $MnV_2O_{6+\delta}$ compounds. The theoretical capacity (+) corresponding to the Mn^{4+}/Mn^{3+} reduction is given for comparison.

It must be pointed out that Q_{irr}* is only one part of the irreversible capacity. As a consequence, other possible phenomena that could account for the remaining part should be discussed: XAS and EELS experiments indicate (vide infra) that an irreversible reduction of V^{5+} can be discarded; and an electrolyte reduction leading to the formation of a passivation layer on the materials is possible. The important variation of the irreversible capacity (not yet explained) with composition could then be related to differences in the morphology of the various $MnV_2O_{6+\delta}$ materials. It has already been shown that the irreversible capacity associated with the formation of a passivation layer on carbonaceous materials strongly depends on their structure and morphology.[41]

The cycling behavior of composite electrodes containing $MnV_2O_{6.9}$ and $MnV_2O_{6.96}$ materials (which exhibit the highest reversible capacities at the first cycle) was tested between 10 mV and 3.9 V in galvanostatic mode over more than 100 discharge−charge cycles at cycling rates of C/6 or C/4 (C/*n* corresponds to a charge or a discharge within n hours). Figure 19 shows that the reversible capacity decreases over the first severals tens of cycles and then increases to reach almost stable values after about 100 cycles.

4.3. Behavior of $MnV_2O_{6.96}$ in a Li Ion Battery. From the electrochemical experiments vs lithium metal performed on the materials, one of them, $MnV_2O_{6.96}$

(41) Dahn, J. R.; Sleigh, A. K.; Hang Shi; Way, B. M.; Weydanz, W. J.; Reimers, J. N.; Zong, Q.; von Sacken, U. *Lithium batteries, New materials, Developments and perspectives*; Pistoia, G., Ed.; Industrial Chemistry Library; Elsevier Science B. V.: New York, 1994; Vol. 5, p 1.

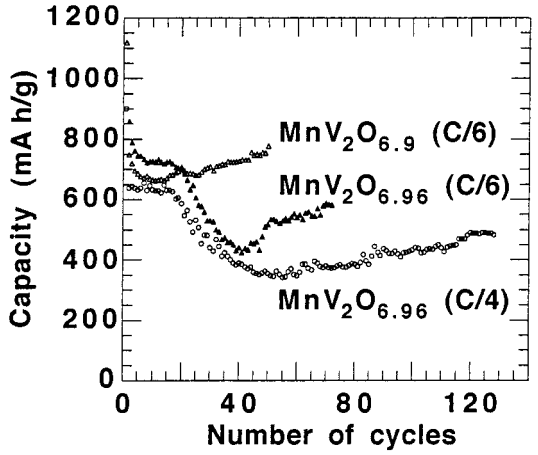

Figure 19. Cycling behavior of $MnV_2O_{6.9}$ at C/6, $MnV_2O_{6.96}$ at C/4 and C/6 in the 3.9−0.01 V voltage range.

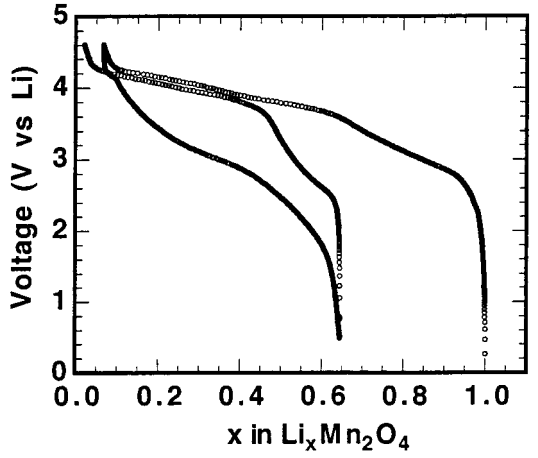

Figure 20. Galvanostatic charge−discharge curves of the Li_x-$MnV_2O_{6.96}$/$Li_{1-x}Mn_2O_4$ cell.

which displays the better Li uptake and cyclability, was chosen as the negative electrode in a Li ion cell with the spinel $LiMn_2O_4$ as the positive. The setup of the cell requires an appropriate amount of material at each electrode to equilibrate the first charge capacity. As previously shown, $MnV_2O_{6.96}$ exhibits a first discharge capacity as high as 1000 mA h/g of electrode material (see Experimental Details for the composite electrode loading), which is an advantage compared to carbonaceous materials. Figure 20 shows the voltage profile curve of the Li ion cell. During the charge, Li ions are extracted from $LiMn_2O_4$ and stored into $MnV_2O_{6.96}$. In the following process, Li ions are released from the negative electrode and stored back into the spinel structure. This swing Li migration is hampered by the irreversible capacity loss occurring at the electrode material, mostly the negative. The irreversible capacity at first cycle for $LiMn_2O_4$ is counting for less than 10%. Then, the observed capacity loss (35%) at first cycle is attributed to the incomplete extraction from $MnV_2O_{6.96}$ due to the high rate of C/5. The specific capacity of our Li ion cell is 78 mA h/g, slightly higher than that in which graphite is used as negative electrode (70 mA h/g). Although our system suffers from a relatively low average discharge voltage, inherent to the high Li releasing voltage for $MnV_2O_{6.96}$, its specific energy is 235 mW h/g, close to that of $LiMn_2O_4$/C (273 mW h/g.

Table 4. Average Oxidation States d_V and d_{Mn} of V and Mn, Respectively, and α Values Describing the Electronic Transfer of Li to the $Li_xMnV_2O_{6.96}$ Host Matrix (Inferred from EELS Experiments)

x in $Li_xMnV_2O_{6.96}$	d_V (±0.2)	d_{Mn} (±0.2)	α[a]	$2d_V + d_{Mn} + x\alpha$
0	5.0	4.0		14.0
7	3.8	2.1	0.70	14.6
10	3.3	2.0	0.60	14.6
4[b]	4.3	2.5	0.80	14.3
1.5[b]	5.0	2.6	0.93	14.0

[a] See text. [b] Sample prepared by a complete discharge + a partial charge.

5. Characterization of the Li Derivatives

The intrinsic reversible capacities of $MnV_2O_{6+\delta}$ materials reach such high values that they formally would correspond to an almost complete reduction of the transition metal cations M. This result raises important questions concerning the evolution of MO_n polyhedra and electronic transfers from Li to the host matrix, to which investigations by local techniques can shed some light.

Therefore, XAS experiments have been undertaken on different $Li_xMnV_2O_{6.96}$ compositions hereafter labeled A, B, ..., E. Materials B−E were obtained from A ($MnV_2O_{6.96}$) after the following electrochemical steps: (1) half a discharge for B (~$Li_6MnV_2O_{6.96}$), (2) a complete discharge for C (~$Li_{12}MnV_2O_{6.96}$), (3) a complete discharge + half a charge for D (~$Li_6MnV_2O_{6.96}$), and (4) a complete discharge−charge cycle for E (~$Li_2MnV_2O_{6.96}$).

Materials corresponding to slightly different compositions (see Table 4) were also investigated by EELS. The energy positions of the Mn and V $l_{2,3}$ edges and the white line l_3/l_2 intensity ratios were used to determine the oxidation state of the TM elements. In the case of vanadium, V_2O_3, $VOSO_4 \cdot 5H_2O$, and V_2O_5 were used as references. The Li k-edge energy was also measured by EELS. As a matter of fact, it has previously been shown that the correlation between the position of the edge and the oxidation state of TM elements can also be extended to the case of Li,[42] which enables the determination of a coefficient α, describing the electronic transfer from Li to an host matrix. This was done with the use of an arbitrary scale taking α as equal to 0 and 1, respectively, for the energy measured with Li metal and Li_2S. The results are reported in Table 4.

5.1. Evolution of the Electronic Transfer from Li to the Host Matrix. As expected, α values reported in Table 4 indicate a decrease of the electronic transfer from Li to the host matrix with increasing the Li content x in $Li_xMnV_2O_{6.96}$. Furthermore, if the positive charge born by Li is taken as equal to α, while those of the transition metal cations are assimilated to their oxidation states (d_{Mn} and d_V for Mn and V, respectively) inferred from EELS experiments, it must be mentioned that the sum of positive charges (see Table 4) in Li_x-$MnV_2O_{6.96}$ balances that of negative ones (2 × 6.96) reasonably well. α values giving an exact balance as well as those determined from a direct measurement of the Li k-edge energy by EELS are represented in Figure 21, to better illustrate a clear decrease of the electronic

(42) Auriel, C. Ph.D. Thesis, Nantes 1993.

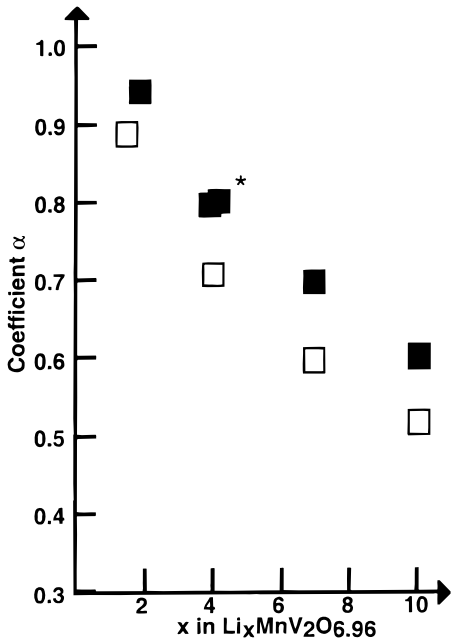

Figure 21. Evolution of α as a function of x in the Li_x-$MnV_2O_{6.96}$ compounds. (α from the electroneutrality eq $2d_V + d_{Mn} + x\alpha = 13.92$ are indicated with open squares; α from a direct measurement of the Li k edge energy, filled squares). (The asterisk indicates a sample prepared by a complete discharge + a partial charge.)

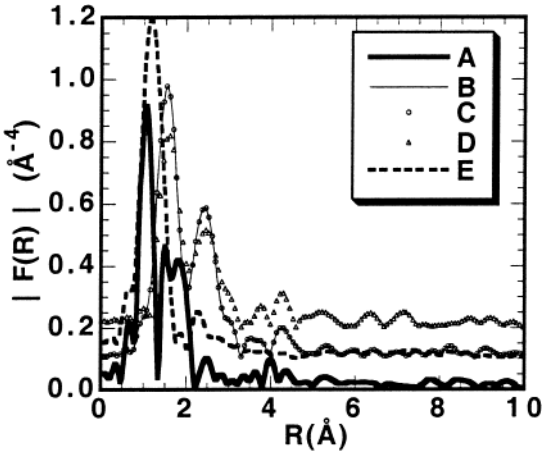

Figure 22. Modulus of the EXAFS spectra Fourier transform (V k edge) of compounds A−E (see text). (The distances are not corrected for atomic potential phase shifts.)

transfer from Li to the host matrix with x, regardless of method is used to determine α.

5.2. Evolution of the V Oxidation State and of the VO_n Polyhedron. For compounds B−E, the presence of a single V−O peak in the RDFs (Figure 22) indicates that after electrochemical treatment the V−O distances become much closer to each other than they were in the starting material A, for which three V−O peaks are observed. These V−O peaks were refined as described above, and the main results are given in Table 5.

For B and D, the V−O distances are 2.02 and 2.03 Å, respectively. It is slightly longer for C, 2.05 Å. In these three cases, the refinement leads to a number of oxygen neighbors close to six, instead of five in compound A. Furthermore, on the XANES spectra of B−D, the preedge peak intensities are much weaker than for A

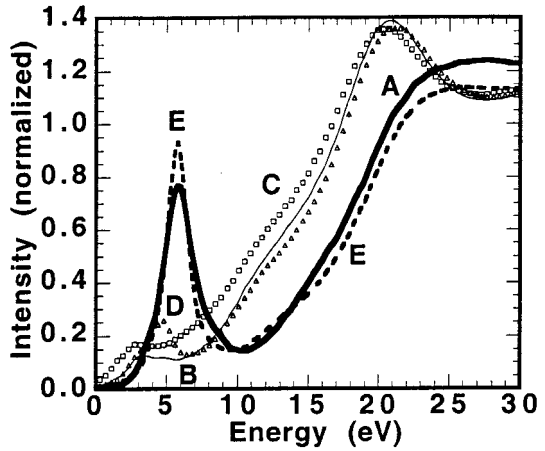

Figure 23. Normalized V k-edge XANES spectra of compounds A−E (see text).

Table 5. Fitting Results for the EXAFS Analysis at the V k Edge for $Li_xMnV_2O_{6.96}$ Compounds

compound[a]	N	V−O (Å)	$\sigma \times 10^{-2}$ (Å)	ΔE (eV)	ρ (%)
A ($x = 0$)	2.0	1.65			
	1.8	1.90	5	8.2	8
	1.0	2.06			
B ($x = 6$)	5.4	2.02	5	6.8	1
C ($x = 12$)	5.3	2.05	5	7.6	5
D ($x = 6$)	5.5	2.03	5	8.6	3
E ($x = 2$)	3.8	1.73	6	8.0	3

[a] See text.

(Figure 23). These results are a clear signature of a 6-fold coordination of vanadium atoms occupying octahedral sites, in B−D compounds.

After a complete discharge−charge cycle (compound E), the V−O distance becomes much shorter, 1.73 Å, and the number of oxygen neighbors is four. The preedge peak intensity (XANES spectrum) is very large, even larger than for the starting material A (Figure 23). Such results are a clear signature of V^{5+} cations in a tetrahedral coordination, in compound E.

On account of these XAS results and of average oxidation states inferred from EELS (Table 4), the following evolution can be proposed for V: upon half a discharge (compound B, $\sim Li_6MnV_2O_{6.96}$), V cations are a mixture of V^{3+} and V^{4+}, exhibit a 6-fold rather symmetrical environment of O atoms (likely to be octahedral). A similar environment is observed for compound C ($\sim Li_{12}MnV_2O_{6.96}$) with an average oxidation state close to +3. During the following charge, V in compound D (half a charge) appears similar to V in B (compounds B and D have the same chemical composition: $\sim Li_6MnV_2O_{6.96}$). However, the small preedge peak observed for D could correspond to a small fraction of V atoms in a tetrahedral coordination. Finally, after a complete discharge−charge cycle (compound E, $\sim Li_2MnV_2O_{6.96}$), V cations come back to the 5+ oxidation and occupy VO_4 tetrahedra.

5.3. Evolution of the Mn Oxidation State and of the MnO_n Polyhedron. X-ray absorption spectroscopy experiments at manganese k edge do not lead to obvious conclusions about the role played by manganese atoms in the cycling behavior. Nevertheless Figures 24 and 25 show clear modifications of both XANES spectra and RDF's upon lithium cycling. The first point is that upon

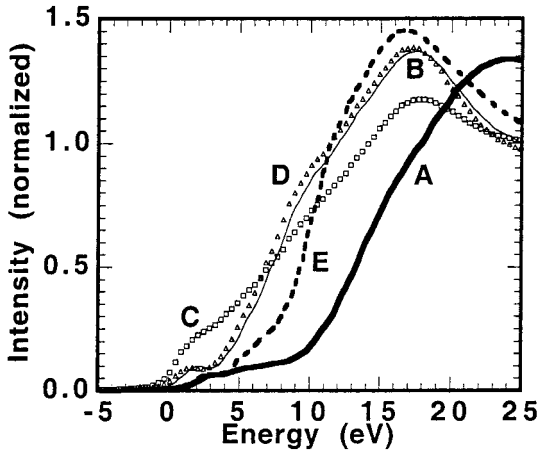

Figure 24. Normalized Mn k-edge XANES spectra of compounds A−E (see text).

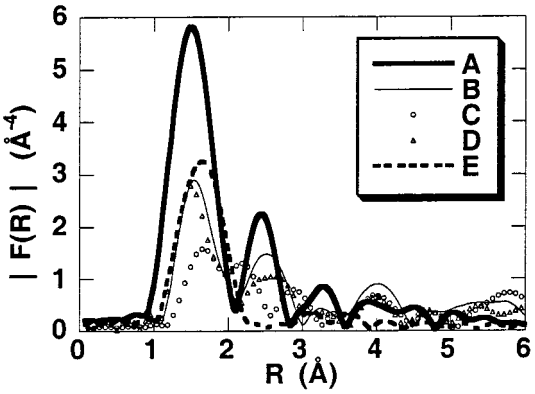

Figure 25. Modulus of the EXAFS spectra Fourier transform (Mn k edge) of compounds A−E (see text). (The distances are not corrected for atomic potential phase shifts.)

lithium reaction the manganese−oxygen distance increases from 1.895 Å in the starting phase, where manganese is at the 4+ oxidation state, to 2.111 Å for compound B (Table 6). This is in a good agreement with the reduction of manganese which has been deduced from EELS experiments (Table 4), and the shift of the main edge toward the lower energies (Figure 24) is a signature of this reduction. For the compounds B, D, and E, the coordination number is very close to six and the Mn−O distance is not significantly modified. Compounds B and D are very similar in both RDF's and XANES spectra but E is different from A. Compound C which corresponds to $x = 12$ is different from B. The coordination has been refined as 4 + 1 with one short (2.012 Å) and four long (2.508 Å) Mn−O distances. We have no explanation for such a surprising result. Compounds A and E do not differ only in the distances and the edge position, but also in the fact that the second coordination peak has completely disappeared after a complete discharge−charge cycle. This is the signature of a completely disordered cationic environment of manganese atoms in E. The fact that C and E differ from B and D proves that even if its oxidation state is not largely modified upon cycling, Mn plays a role in the process, at least for participating in the "structure", and enables V to play the crucial role in the charge-transfer process. It is also remarkable that the Debye−Waller terms are much larger in the cycled compounds (Table 6) as compared to the pristine one,

Table 6. Fitting Results for the EXAFS Analysis at the Mn k Edge for $Li_xMnV_2O_{6.96}$ Compounds

compound[a]	*N*	Mn−O (Å)	$\sigma \times 10^{-2}$ (Å)	ΔE (eV)	ρ (%)
A ($x = 0$)	4.2	1.895	7.9	6.50	0.8
B ($x = 6$)	6.0	2.111	13.6	3.64	1.5
C ($x = 12$)	0.8	2.012	4.7[b]	9.82	1.2
	4.3	2.510	23.6[b]	10.27	
D ($x = 6$)	6	2.096	14.0	3.92	1. 6
E ($x = 2$)	6	2.116	12.1	2.68	2. 9

[a] See text. [b] Parameters for an anharmonic distribution of the distances.

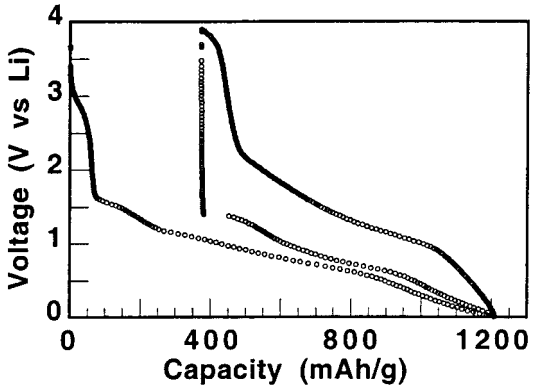

Figure 26. Voltage−capacity curves for composite electrodes $CoV_2O_{6.16}$ + C (10 wt %).

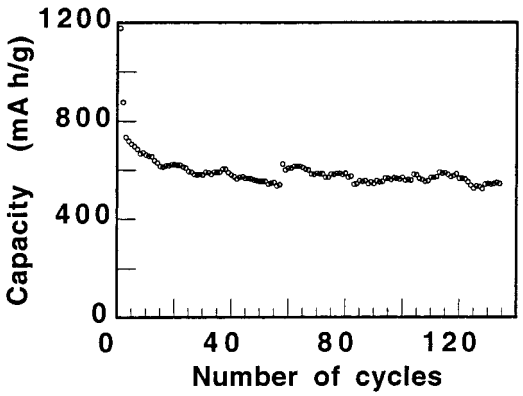

Figure 27. Cycling behavior of $CoV_2O_{6.16}$ at C/6 in the 3.9−0.01 V voltage range.

regardless of their lithium content. This is the signature of a large distribution of Mn−O distances. Moreover for compound C we had to introduce an anharmonic distribution of these distances. This fact corresponds, at least for the manganese environment, to an extremely disordered case.

6. Preparation and Electrochemical Behavior of Amorphous $CoV_2O_{6+\delta}\cdot nH_2O$

Taking into account that the crystal structure of $CoV_2O_6\cdot 4H_2O$[43] is isotopic with that of $MnV_2O_6\cdot 4H_2O$, the ozonation of the crystallized Co precursor was undertaken at 95 °C. After this treatment, the material was amorphous. Characterization of this material (chemical and spectroscopic analyses) is in progress; however, from TG experiments a $CoV_2O_{6.26}\cdot 5.3H_2O$ composition

(43) Avtamonova, N. V.; Trunov, V. K.; Bekrukov, I. Ya. *Izv. Akad. Nauk SSSR, Neorg. Mater.* **1990**, *26*, 346.

can already be proposed. Simultaneously, electrochemical experiments have been carried out under conditions similar to those already used for $MnV_2O_{6+\delta}$ materials. A typical chronopotentiometric curve is displayed in Figure 26. As in the case of $MnV_2O_{6.96}$, no Li uptake occurs above 1.7 V (vs Li). The composite electrode containing carbon black (10% in weight) exhibits a large capacity during the first discharge. The following cycles are almost perfectly reversible as indicated by Figure 27 which gives the evolution of the reversible capacity over more than 130 discharge−charge cycles at a cycling rate of C/6.

These preliminary results show that the synthetic route leading to $MnV_2O_{6+\delta}\cdot nH_2O$ materials can be extended to other vanadium oxide-based hydrated precursors leading to materials with the peculiar property of reversibly storing large amounts of Li at low voltage vs Li.

7. Conclusion

The characterization of $Li_xMnV_2O_{6.96}$ compounds at various steps of the discharge/charge process shows that the electron storage mechanism does not correspond to a depletion of the materials into a mixture of Li_2O and metallic TM, as was proposed for some iron oxides.[44] However some features of the electrochemical behavior (e.g., the large voltage difference between discharge and charge) indicate that this mechanism is not a classical intercalation reaction either.[45] Various vanadates exhibiting very large Li storage capacities at low voltage (a behavior very similar to that of the title compounds) have been investigated recently.[10] A storage mechanism was proposed involving the formation of Li−O bonds on the unshared oxygen atoms of the first coordination shell of V cations.

CM991074G

(44) Thackeray, M. M.; David, W. I. F.; Goodenough, J. B. *J. Solid State Chem.* **1984**, *55*, 280−286.

(45) Legrand, A. P., Flandrois, S., Eds. *Chemical Physics of Intercalation*; NATO ASI Series; Plenum Press: New York, 1987.